J. Fluid Mech. (2005), *vol.* 537, *pp.* 387–413. © 2005 Cambridge University Press
doi:10.1017/S0022112005005306 Printed in the United Kingdom

Experimental and numerical investigation of the dynamics of an underwater explosion bubble near a resilient/rigid structure

By E. KLASEBOER[1], K. C. HUNG[1], C. WANG[1], C. W. WANG[1], B. C. KHOO[2,3]†, P. BOYCE[4], S. DEBONO[4] AND H. CHARLIER[5]

[1]Institute of High Performance Computing, Science Park Road, 01-01 The Capricorn, Singapore Science Park II, Singapore 117528

[2]Singapore MIT Alliance, 4 Engineering Drive 3, Singapore 117576
mpekbc@nus.edu.sg

[3]Department of Mechanical Engineering, National University of Singapore, Kent Ridge, Singapore 119260

[4]Centre Technique Des Systèmes Navals, BP 28, 83800 Toulon Naval, France
ph.boyce@ctsn.dga.defense.gouv.fr

[5]ESI SOFTWARE SA, 99 rue des Solets, SILIC 112, 94513 Rungis Cedex, France
Herve.Charlier@esi-group.com

(Received 19 October 2004 and in revised form 14 March 2005)

This paper deals with an experimental and numerical study of the dynamics of an underwater explosion and its associated fluid–structure interaction. Experimental studies of the complex fluid–structure interaction phenomena were carried out in a specially designed test pond. The pond is equipped with a high-speed camera and pressure and displacement sensors. The high-speed camera was used to capture the expansion and collapse of the gas bubble created by the explosion. Several different structures were used in the experiments, including both rigid and resilient plates of circular shape. The deformation of the plate was measured with a non-contact laser telemetry device. The numerical simulations of the explosion bubble interacting with a submerged resilient structure were performed using a three-dimensional bubble dynamics code in conjunction with a structural code. The bubble code is based on the boundary-element method (BEM) and has been coupled to a structural finite-element code (PAM-CRASH^{TM}). The experimental results were compared against the numerical results for different bubble–structure configurations and orientations. Several physical phenomena that have been observed, such as bubble jetting and bubble migration towards the structure are discussed.

1. Introduction

The underwater detonation of an explosive can have serious effects on a nearby structure (such as a ship or submarine). The same amount of explosive can cause greater damage underwater than it would have caused in air, because water is much less compressible than air. The physics of an underwater explosion are complex and many phenomena can be encountered from combustion and shock waves to structural mechanics. The response of the structure is determined by a number of factors, such as the density, strength and thickness of its constituent material.

† Author to whom correspondence should be addressed.

Just after the detonation, a shock wave and an expanding high-pressure gas bubble will appear. This shock wave moves at a very high speed and will generate a very high pressure. When it hits the structure, it gives rise to the first damaging mechanism. While the pressure loading due to the shock impact can be very high, the duration is usually very short compared with the dynamics of the bubble. The explosive products form a high-pressure gas bubble and this bubble expands owing to the high pressure. However, inertia causes the bubble to overexpand and the pressure inside the bubble becomes lower than the surrounding reference pressure; it then stops expanding (for example, the maximum bubble diameter in a typical explosion of a torpedo of 500 kg TNT is of the order of 10 to 20 m). The hydrostatic pressure is now larger than the pressure inside the bubble and a collapse phase will follow. If the frequency of the bubble 'matches' the eigenfrequency of the structure, it can lead to the so-called 'whipping' effect which can potentially constitute the second damaging mechanism. In most cases, in the collapse phase, the attraction of the bubble towards the structure (Bjerknes effect), the influence of gravity and inertia will cause a high-speed water jet to develop. The jet traverses the bubble and impacts on the other side of the bubble surface. This jet can be directed towards the structure and is then associated with a third damaging mechanism. After jet impact, the bubble will become toroidal in shape and will continue to contract. Not long after the jet impact, the bubble reaches its minimum volume and a high-pressure peak can be observed. The bubble will then rebound again for a second cycle. It will have lost much of its energy and the second cycle is less 'violent'.

In the last few decades, the boundary integral method (BEM) has been widely applied to simulate bubble dynamics problems. Bubbles of all sizes have been simulated, from large explosion bubbles to small cavitation bubbles. The BEM reduces the dimension of the problem by one, since only the boundaries of the problem need to be meshed, with the fluid domain remaining mesh-free. Another advantage of the BEM is that the mesh can follow the deformations of both bubble and structure well, even if the bubble becomes highly distorted. The employment of the BEM in bubble dynamics can be seen in Blake & Gibson (1981) who studied the growth and collapse of a vapour cavitation near a free surface. Their numerical results of the bubble shape as it evolved matched well with the experiments, which suggests that BEM can be a valid approach to capturing the complex features of bubble dynamics including the formation of a water jet. Blake & Gibson (1987) studied cavitation bubbles near solid boundaries. They introduced a criterion to calculate the time-step size for bubble dynamics problems by simply allowing the potential to change by only a prescribed amount anywhere on the mesh between two time steps. Other works employing the BEM to study bubble dynamics include Oguz & Prosperetti (1990)'s investigation of the entrained bubbles produced by the impact of drops on the surface of the same liquid. Lundgren & Mansour (1991) used the BEM to study initial spherical and toroidal bubbles rising in a gravity field. The three-dimensional motion of a bubble close to a fixed rigid structure was simulated by Harris (1992); this study was limited to simulations prior to jet impact. Zhang, Duncan & Chahine (1993) simulated an initially spherical cavity bubble located near a rigid wall until its toroidal phase. In their computation, a layer was defined to separate the water jet and the surrounding domain during the toroidal bubble phase. This layer acts as a vorticity sheet and moves with the flow. The layer deforms as much, if not much more than the bubble surface, which can make the tracking very challenging. Zhang & Duncan (1994) extended their study to cover gas bubbles. In a parallel development, Wang *et al.* (1996) studied the nonlinear interaction between a gas bubble and a free surface.

They employed a so-called surgical-cut to convert the originally simply-connected bubble to a toroidal shape after the jet impact. Instead of adding a vortex sheet at the impact area, a vortex ring was placed inside the bubble to account for the double connectivity of the bubble. There is no longer the need for meticulously tracking the vorticity sheet as in Zhang *et al.* (1993); we just ensure that the vortex ring stays inside the toroid as the bubble evolves. However, their simulations were limited to axisymmetrical configurations. Tong (1997) numerically investigated the interaction of transient cavities in fluid flows with rigid boundaries, using the image method; the boundary is therefore not discretized and is infinite and flat. Zhang *et al.* (1998) did a three-dimensional computation to study the dynamics of bubbles and a free surface. In their work, several configurations of two bubbles were calculated to understand better the underlying flow physics. Zhang *et al.* (2001) extended the surgical-cut and vortex ring technique to general three-dimensional toroidal bubble problems, looking specifically at the issues of the physical impact and its relation to the numerical stability of the BEM code. Other methods, such as the finite-volume formulation of Popinet & Zaleski (2002) were also used to simulate oscillating bubbles near a solid surface.

The work of Cole (1948) still contains much useful data concerning experimental and simple theoretical modelling of underwater explosions. In recent decades, with the advances in numerical techniques and experimental equipment such as high-speed cameras, several attempts to capture the behaviour of bubble dynamics have been made. Though most of these works were numerical, some experimental data do exist. Tomita, Shima & Takahashi (1983) studied the collapse of a small gas bubble attached to a solid wall induced by a shock wave. At about the same time, Shima, Takayama & Tomita (1984) experimentally investigated, in fair detail, the collapse of a single spark-generated cavitation bubble near a solid wall with different stand-off configurations. Shima *et al.* (1989) studied the growth and collapse of a bubble near a composite surface consisting of two viscoelastic materials. Tomita, Shima & Takahashi (1991) experimented on the behaviour of a bubble near a rigid wall (with two kinds of axi-symmetrical shape). Tipton, Steinberg & Tomita (1992) made an experimental and numerical study on an expanding and collapsing bubble in the vicinity of a rigid wall. Their bubbles were very small (a few mm) and generated by electric sparks. These sparks create difficulties in estimating the initial size, shape and energy of the bubble. According to Tipton *et al.*, if a small amount of high explosive were used (as in our experiments), the geometry, density and initial energy of the bubble could be specified much better. They also made some comparisons of their experimental data to computations. Tomita *et al.* (1994) investigated the dynamics of motion of a laser-generated bubble in liquid nitrogen using high-speed photography. Tomita & Shima (1994) experimentally studied the interactions between a bubble and a boundary, bubble–bubble interaction and shock wave–bubble interaction. Chahine *et al.* (1995) conducted some tests with spark-generated bubbles. Finally, Brett, Yiannakopoalos & Schaaf (2000) did some experiments to measure the deformation of submerged cylinders subject to loading from a nearby explosion. All these above mentioned experiments are confined to rather small bubbles and not large explosion bubbles, with the possible exception of Brett *et al.* (2000). Unfortunately, for the latter, their objective and emphasis is on the final structural deformation and not on the bubble dynamics *per se*, so no direct measurements concerning bubble properties are reported.

In the present study, the intention is to investigate experimentally and numerically the interaction (and main physics) between an underwater explosion bubble and a

nearby submerged structure, both rigid and resilient. To our knowledge, this is one of the first times that results concerning bubble dynamics and structural deformation in a underwater explosion test have been described and made available in the open literature. Experiments were performed at the CTSN (Centre Technique des Systèmes Navals) test pond, specially designed for detonation trials, in Toulon, France. Several charge weights and stand-off distances were employed. The single explosive composition used is Hexocire (RDX + wax). More than 18 tests were performed, among them free-field explosions and explosions near horizontal and vertical plates. In our numerical study of the bubble dynamics, the response of the structure to the shock wave is not considered. This is justified because the duration of the shock is usually very short and the inertia of the structure is too large for it to respond significantly. The water surrounding the bubble and structure is assumed to be incompressible and irrotational and the BEM is applied. When the bubble forms a toroidal shape, after jet impact, the rotational part of the flow is represented by a vortex ring of known strength which is located inside the bubble, but the remaining flow is still irrotational, similar to numerous previous studies. An elastic–plastic deformation model is used for the structure, which is calculated by a nonlinear finite-element method (FEM) structural solver (PAM-CRASH^{TM}). In order to obtain the dynamic interaction between bubble and structure, the computation of the bubble dynamics must be coupled with the simulation of the structural deformation. It is done by exchanging information (position and forces) between the BEM solver and the FEM solver on the nodes of the structure (the so-called wetted surface). Comparisons, both qualitatively and quantitatively between the results of the experiments and numerics are made.

2. Experimental set-up

Experiments with reasonably small test charges near submerged resilient structures were carried out by the Centre Technique des Systèmes Navals in France in a specially designed test pond. The pond has a truncated cone shape with a mean radius of 9 m at the top surface, a depth (H_{pond}) of 7 m and a useful mean radius (R_{pond}) of 7.5 m at mid-depth. A high-speed camera (1000 images s^{-1}) is used to record the explosion bubble phenomena. A special device consisting of mirrors and tubes has been used to protect the camera from the hazardous effects of the explosion (the camera is placed above the waterline). All explosions were performed at a depth of 3.5 m (the explosive device is placed roughly at the middle of the pond). The sidewalls of the pond have steps cut in and are covered with sacks of railway track ballast, held in place by a wire netting framework. This design effectively diffracts the shock waves induced by the explosion and also absorbs the bulk of the explosion energy. The maximum bubble radius for an explosive of 55 g is $R_m = 0.54$ m. The radius of the pond compared to the radius of the bubble is now: $R_m/R_{pond} = 0.072$. Half the depth of the pond compared to the radius of the bubble is $2R_m/H_{pond} = 0.15$. These values are sufficient to ensure that the boundaries and the free surface of the pond do not greatly influence the bubbles' behaviour. The single explosive composition used in these experiments is Hexocire (RDX + wax), with charge weights of 10 g, 35 g and 55 g. The charge is detonated using an exploding bridgewire detonator (without primary explosive) and a high-energy unit. This is a device which provides the detonator with a very high voltage pulse from the main power supply. Tourmaline piezoelectric pressure sensors are used to measure the time history of the pressure in the fluid and on the plate. The small and robust tourmaline crystal is able to withstand high dynamics pressures of

more than 100 MPa. The deflection of the resilient plate is measured as a function of time using a non-contact laser telemeter device installed on the supporting structure called MEDUSE. MEDUSE is a rigid structure weighing up to two tons. It has been designed to study the fluid–structure interaction caused by an underwater explosion near an air-backed structure. MEDUSE can be lifted out of the water to perform the necessary arrangements before the start of an experiment. During the experiment, MEDUSE is suspended on buoys. The inertia of MEDUSE is such that for charges lesser than 200 g, it can be considered as fixed in space. Direct sunlight was also used as a light source in the experiments.

3. Theory and numerical modelling

3.1. *Introduction*

The numerical calculations can be split into two parts: the fluid part and the structural part. The fluid part is carried out using the boundary integral method. Special care must be taken after the jet impact, induced by the collapsing bubble, since the fluid domain then becomes doubly connected; a vortex ring is placed inside the bubble to account for this. The structural part is solved using the finite-element solver PAM-CRASH^{TM}. A 'loose' coupling between the two codes has been made; information concerning displacements of the structure are passed on from the structural code to the fluid code and forces (deduced from the pressure loading on the structure) are passed on from the fluid code to the structural code. A controlling interface code decides which code has to be called to do the appropriate calculations and making the relevant results available as input to the other code. Time steps and structural meshes can be different for the two codes.

3.2. *Boundary-element method (BEM) for the fluid part*

The assumption that the fluid is inviscid and incompressible and the induced motion is irrotational indicates that there exists a potential function $\phi(x, y, z)$ in the fluid domain which may be bounded by bubbles and/or structures. For an explosion bubble of relatively large dimensions, inertia is the main governing parameter as opposed to the viscous effect and hence the absence of viscosity in our computation is reckoned not to affect significantly the primary flow physics. The problem under consideration is an external problem (i.e. the fluid extends to infinity). The velocity vector can be derived from this potential as: $\boldsymbol{u} = \nabla\phi$. These assumptions are clearly not valid just after the detonation (shock waves are not described by potential theory). However, the effects of the shock wave are short-lived and do disappear relatively quickly and probably do not significantly influence the solution associated with the bubble dynamics where the potential theory is assumed to be valid. It is noted in Cole (1948) that the event of shock dynamics occurs in the order of milliseconds after the detonation, while the duration of the flow physics of the bubble are measured in seconds. A Cartesian coordinate system O_{xyz} is used with the z-axis pointing in the opposite direction to the gravity acceleration vector. Green's second identity reads

$$c(\boldsymbol{x})\phi(\boldsymbol{x}) + \int_s \left[\phi(\boldsymbol{y})\frac{\partial G(\boldsymbol{x}, \boldsymbol{y})}{\partial \boldsymbol{n}(\boldsymbol{y})} - \frac{\partial \phi(\boldsymbol{y})}{\partial \boldsymbol{n}(\boldsymbol{y})} G(\boldsymbol{x}, \boldsymbol{y})\right] \mathrm{d}s(\boldsymbol{y}) = 0, \tag{1}$$

where $\boldsymbol{x}$ is a vector pointing to a control point situated on the boundary S; $\boldsymbol{y}$ is a vector pointing to an integration point; $G(\boldsymbol{x}, \boldsymbol{y}) = 1/|\boldsymbol{x} - \boldsymbol{y}|$ is the free space Green's function; $c(\boldsymbol{x})$ is a geometrical parameter associated with the solid angle, and $\boldsymbol{n}(\boldsymbol{y})$ is the unit normal vector pointing out of the fluid domain. The normal derivative is

defined as: $\partial/\partial \boldsymbol{n} = \boldsymbol{n} \cdot \nabla$. The integration in (1) has to be performed on all surfaces (indicated by S): on the bubble and the structure. Thus, only meshes on the surfaces of the bubble and structure are required. A non-condensable gas that obeys the adiabatic gas law (vapour pressure is ignored) is assumed to form the contents of the bubble:

$$P = P_0 \left(\frac{V_0}{V} \right)^{\lambda}, \tag{2}$$

where V_0 and P_0 are the initial volume and pressure, respectively, of the non-condensable gas. The constant ratio of specific heats is indicated by λ, which is equal to 1.25 for the gaseous explosion products resulting from an TNT explosion (see Cole 1948). It is reckoned that the overall bubble dynamics are sufficiently fast and the bubble size sufficiently large to prevent significant exchange of heat from the bubble to the surrounding fluid and hence the adiabatic condition (2) is imposed. We may note too that the response time of the compressible air within the bubble is much smaller when compared to that of the external fluid. Therefore, the flow inside the bubble can be considered to be in equilibrium. All variables are then converted to dimensionless variables with respect to the length scale R_m (the Rayleigh bubble radius, corresponding to the maximum radius of a similar spherical symmetrical bubble having the same initial size and pressure placed in an infinite fluid without gravity), the reference pressure P_∞ and the time scale $R_m\sqrt{\rho/P_\infty}$. The reference pressure P_∞ is defined as the pressure at infinity on the O_{xy} coordinate plane located at the initial bubble centre. With this time scale, the dimensionless time unit '1' represents roughly half the oscillation time of a bubble (from initial state to maximum bubble size). The dimensionless unsteady Bernoulli equations are, neglecting the surface tension on the bubble–water interface:

$$\frac{\partial \phi}{\partial t} = 1 - \tfrac{1}{2}|\boldsymbol{u}|^2 - \delta^2 z - P \qquad \text{on the wetted surface of the structure,} \tag{3}$$

$$\frac{\partial \phi}{\partial t} = 1 - \tfrac{1}{2}|\boldsymbol{u}|^2 - \delta^2 z - \varepsilon \left(\frac{V_0}{V} \right)^{\lambda} \qquad \text{on the bubble surface,} \tag{4}$$

with $\delta = \sqrt{\rho g R_m / P_\infty}$ being the buoyancy parameter and $\varepsilon = P_0/P_\infty$ being the strength parameter as denoted by the ratio of the initial bubble pressure and ambient pressure. The parameters ε and R_m (dimensional) are obtained from empirical relationships, based on field trials/experiments collected over the years, requiring only the TNT equivalent weight and the initial depth of the explosive, see for example Rungsiyaphornrat *et al.* (2003). These relationships were determined for large-scale underwater explosions. One such a relation can be found in Cole (1948), relating the initial gas pressure to the weight of the charge (W). In SI units this relationship reads:

$$P_0 = 1.39\,10^5 (W/V_0)^{\lambda}. \tag{5}$$

Another empirical relationship follows from the fact that the maximum volume of the bubble is proportional to the charge weight and inversely proportional to the hydrostatic pressure (depending linearly on the charge depth Z); this will lead to the following relationship for the maximum bubble radius:

$$R_m = 3.38 \left(\frac{W}{Z + 10} \right)^{1/3}. \tag{6}$$

The bubble is assumed to be spherical at the beginning of the numerical calculations and its radius is set to R_0, (obtained from V_0). The three parameters R_0, λ and ε can not be chosen independently, but are related by:

$$\frac{\varepsilon}{\lambda - 1}\left(R_0^{3\lambda} - R_0^3\right) = -1 + R_0^3. \tag{7}$$

Equation (7) can be deduced from the Rayleigh–Plesset equation for spherical oscillating bubbles. If (7) is not satisfied, the maximum dimensionless bubble radius will not be 1.0. The surface of the bubble and structure is discretized into a series of three-dimensional linear triangular elements. The bubble consists of 362 nodes and 720 elements using an icosahedron as explained in Wang (1998). The mesh for the solid has a comparable number of nodes and elements (depending on the case). The integrals in (1) are carried out for each triangle. Linear interpolation functions are used for the coordinates, the potential and normal velocity. Each triangle is transformed to a unit triangle and a 7-node Gaussian integration formula is used to calculate the integrals. The resulting contributions are added up for each node which gives rise to a system of linear equations relating $\partial\phi/\partial n$ and ϕ at all nodes of the mesh. For more details on the numerical integration, we can refer to the work by Wang (1998). On the bubble surface, the positions and the potentials of each node can be calculated with the positions and potentials at the previous time step and (4). The positions of each node on the mesh are now updated using a particle-tracing Lagrangian scheme with Eulerian time stepping:

$$\boldsymbol{x}^{t+\delta t} = \boldsymbol{x}^t + \delta t\, \boldsymbol{u}_{EMT}. \tag{8}$$

The nodes are moving with a velocity $\boldsymbol{u}_{EMT}$, which is an optimized velocity in order to keep the mesh regular (see § 3.3 for more details). Note that this velocity is not the material velocity in general. The potential can be updated in a similar way, using the Bernoulli equation:

$$\phi^{t+\delta t} = \phi^t + \delta t \left(1 - \tfrac{1}{2}|\boldsymbol{u}|^2 - \delta^2 z - \varepsilon\left(\frac{V_0}{V}\right)^{\lambda} + \boldsymbol{u}_{EMT}\cdot\boldsymbol{u}\right). \tag{9}$$

To maintain numerical stability, the time-step size δt is chosen in accordance with the following criterion, based on the Bernoulli equation (fairly similar to Blake & Gibson 1987, or Harris 1992):

$$\delta t = \frac{\Delta\phi}{\max\left|1 + \tfrac{1}{2}|\boldsymbol{u}|^2 + \delta^2 z + \varepsilon\left(\frac{V_0}{V}\right)^{\lambda}\right|}. \tag{10}$$

This criterion limits the maximum change in any nodal potential at each time step to a specified constant $\Delta\phi$; the maximum in the denominator of (10) is taken over all the nodal points on the bubble and structure. A value of $\Delta\phi = 0.03$ is used in the computations, being a good compromise between stability and computational efficiency. On the structure, the normal velocity is known. The matrix equation resulting from (1) is solved iteratively to give the normal velocity on the bubble and the potential on the structure. Then, the potential as well as the normal velocity are known on every node for the bubble and the solid. The normal vector can be determined easily on each triangular element. However, the normal vector on each individual node is not yet determined and an approximation has to be found. Invariably, there will be several triangular elements which surround a particular node

and each has a different normal vector. A weighted average scheme, as introduced by Zhang *et al.* (2001), is used to obtain such an approximation; the normal vectors of the surrounding elements $\boldsymbol{n}_i$ are averaged with the inverse of their area S_i:

$$\boldsymbol{n} = \frac{\sum_i \dfrac{\boldsymbol{n}_i}{\Delta_i}}{\sum_i \dfrac{1}{\Delta_i}}. \tag{11}$$

The inverse of the area is believed to be a better weighted average than the area itself; a small element will be nearer the desired node and yield a much better approximation than a larger element. At this point, only the normal velocity is known. The full velocity vector at any node can be obtained with the help of the potential of its neighbouring nodes in a similar way to the normal vector. The detailed procedure has been described in Zhang *et al.* (2001); an estimation for the gradient of the potential (or velocity) can be made from the potential of the nodes of each element i surrounding a particular node. A weighted average scheme similar to (11) can now be applied to find the velocity $\boldsymbol{u}$ at each node:

$$\boldsymbol{u} = \frac{\sum_i \dfrac{\boldsymbol{u}_i}{\Delta_i}}{\sum_i \dfrac{1}{\Delta_i}}. \tag{12}$$

With this velocity known, the pressure anywhere on the structure can be obtained from (3). The time-step size, imposed by (10) seems insufficient to prevent any instabilities from appearing in the simulation (especially during the jet formation). Therefore, a least-squares smoothing scheme is applied at every 10 time steps before jet impact. This scheme is implemented on the potential ϕ as well as the coordinates of the bubble. The values of all the neighbours (n) and the neighbours of the neighbours (m) of a particular node (referred to as 1 in the discussion below) are used in this scheme. A smoothed surface is then represented by a biquadratic function,

$$\tilde{z}' = a_1 x'^2 + a_2 x' y' + a_3 y'^2 + a_4 x' + a_5 y' + a_6 \equiv f(x', y'), \tag{13}$$

where the coefficients, $a_i (i = 1, \ldots, 6)$ are found by minimizing the error function,

$$\boldsymbol{L}(a_1, \ldots, a_6) = \sum_{j=1}^{m+n+1} [f(x'_j, y'_j) - z'_j]^2, \tag{14}$$

where the sum of squares is taken over all the nodal points in the surface patch. After a_i are found, the corrected or smoothed coordinates of the central node 1 is then set to $(0, 0, a_6)$. A more detailed explanation of this smoothing scheme can be found in Zhang *et al.* (2001). If the bubble approaches the structures too closely, numerical instabilities can also occur. Physically, a bubble cannot expand beyond the structural surface and a thin film of fluid always exists between the surfaces of the bubble and the structure. As our intention is not on the physics of the lubricating-like flow between the two said surfaces, but on the primary flow features of the bubble behaviour in the vicinity of the structure, it seem reasonable to set a minimum dimensionless distance of say 0.05 where the bubble surface is not allowed to come closer to the surface. In this way, the bubble can continue to evolve to further elucidate the flow physics especially for the bulk of the main bubble surfaces not directly facing the structural surface.

3.3. *The elastic mesh technique (EMT)*

A feature that has shown its usefulness recently is the elastic mesh optimization technique (EMT, see Wang *et al.* 2003). In many previous work (e.g. Harris 1992; Zhang & Duncan 1994; Zhang *et al.* 2001), the mesh on the bubble is advanced using the material velocity. This results in too many nodes accumulating in the jet tip, while other areas correspondingly have a much lower node density. Zhang *et al.* (2001) suggested maintaining the regularity of the mesh by adding nodes in the sparse areas. It is found that this methodology can introduce numerical problems. The constant node adding in the sparse region will also significantly increase the total number of nodes, which will make the computations very slow. A new mesh regularity control method, or EMT, was introduced by Wang *et al.* (2003). EMT is a mesh regulation technique, which is based on the assumption that the segments of a mesh are elastic (as if elastic springs were attached at each side of a triangular mesh element). EMT can be employed in conjunction with the BEM for the simulation of three-dimensional bubble dynamics in which problems relating to severe mesh distortion as the bubble evolves are a common occurrence. With EMT, the mesh is advanced not by the material velocity, but the optimum shift velocity $\boldsymbol{u}_{EMT}$ obtained by minimizing the total elastic energy stored in every segment of the mesh at each time step; see (8) and (9). In doing so, the same number of nodal points is maintained (at least up to the jet impact). Note, that if we choose $\boldsymbol{u}_{EMT} = \boldsymbol{u}$, (9) will become the discretized Bernoulli equation for a particle moving with the flow. Towards the later part of the simulation, when the jet has been largely developed and just before jet impact, the employment of the EMT method will generally not lead to a more satisfactory mesh redistribution. We therefore switch back to updating the nodes with the material velocity $\boldsymbol{u}$. EMT must be applied earlier on to be most effective in ensuring a more uniform mesh distribution. On the other hand, at this later stage without EMT, the node density is becoming higher at the jet tip, which leads to a better resolution of the flow physics in this region with a large velocity gradient.

3.4. *Jet impact and toroidal bubble formation*

When the jet impacts on the other side of the bubble, numerically a 'hole' must be made to allow the fluid to go through. The issue is to determine when and where an impact is going to take place. We must, therefore, determine which node is situated on the jet-tip. The jet is formed in the final stages of the collapse phase. The dimensionless oscillation time of a bubble is roughly twice the Rayleigh collapse time for a vapour bubble or $2 \times 0.915 = 1.83$. However, in the presence of a structure, the oscillation time of the bubble is slightly increased by about 5–10 % (depending on the standoff distance). In all our simulations, no jet formation has been observed prior to a dimensionless time of $t = 1.95$. To calculate beyond jet impact, the following procedures are adopted when the dimensionless time reaches 1.95. First, the Kelvin impulse vector is computed according to $\boldsymbol{K} = \int_{S_{bubble}} \phi \boldsymbol{n} \, \mathrm{d}S$. We note that the integral is only performed on the bubble surface S_{bubble}. The resulting Kelvin impulse vector will, in general, be pointing in the direction of the jet. We also identify the maximum velocity, $\boldsymbol{u}_{max}$, developed at the bubble surface. A subset of nodes is then created, consisting of all the nodes with a velocity larger than 0.5 $\boldsymbol{u}_{max}$, which encompasses the nodes in the vicinity of the jet-tip. The maximum of the inner product of the position vector $\boldsymbol{x}$ at each node of this subset and $\boldsymbol{K}$ will point to the node which is most advanced on the jet tip (not necessarily the node with the maximum velocity). This node will be labelled J. To illustrate this, consider a typical example of a jet approaching the opposite side of the bubble as in figure 1, which shows an oscillating

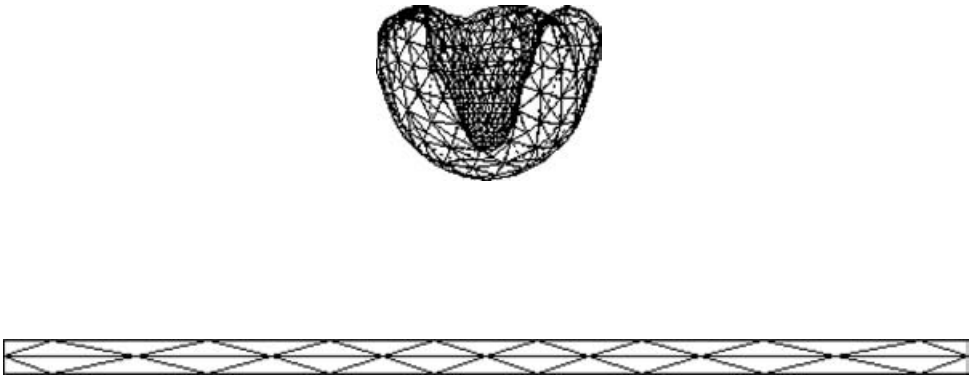

FIGURE 1. A bubble collapsing near a solid square plate.

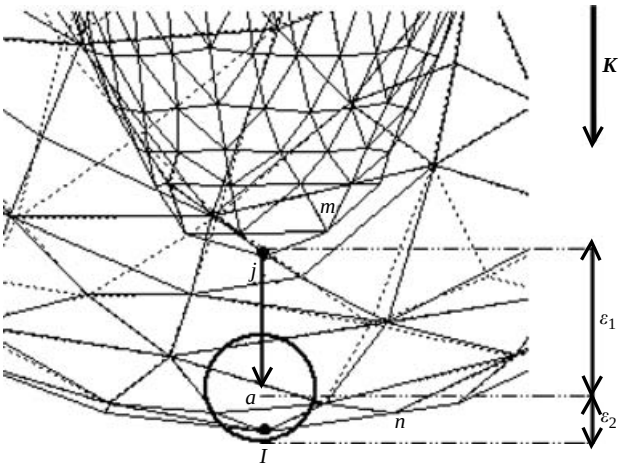

FIGURE 2. The identification of the jet tip node I and the impact node J; I and J will be joined if a sphere around a vector pointing in the jet direction encounters a node on the opposite bubble surface. The Kelvin impulse vector is directed downwards.

bubble located above a rigid square plate. A close-up of the jet tip is given in figure 2 with the node J as indicated. Here, the Kelvin impulse vector is directed towards the plate. As time progresses, we have to establish if, and where, this node is going to impact on the opposite bubble surface. In this respect, we create an artificial point labelled a at a distance ε_1 in the direction of the Kelvin impulse vector (at the end of the arrow starting in node J in figure 2). An artificial sphere is formed around point 'a' as indicated in Figure 2. The radius of this sphere, ε_2, is chosen to be 0.05 times the equivalent diameter of the bubble (in this way, ε_2 will always be larger than the average mesh size). As the value of ε_1 varies from a value slightly larger than ε_2 to 1.0, the artificial sphere advances towards the opposite bubble interface. If a certain node I of the opposite bubble mesh falls inside this sphere, the jet can be expected to impact on this node. The impact criterion is specified such that if the distance between nodes I and J is smaller than a certain value multiplied by the equivalent bubble diameter, the jet is considered to have impacted on the opposite bubble surface. If this impact criterion has not yet been met, we proceed with the next time step, where the same procedure for the updated bubble surface will be repeatedly applied until

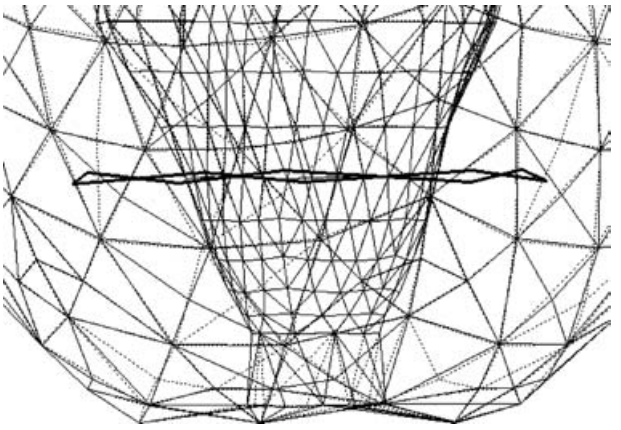

FIGURE 3. A close-up view of the surgical cut, the vortex ring has been placed inside the bubble (indicated above as an almost horizontal line).

the criterion is met. It might seem easier to check the distances between every node on the bubble, but with the above procedure we seek to avoid having 'false' impact nodes from the neighbours of node J (this would mean that the jet impacts on itself). The above procedure is fully automated, in contrast to that described in Zhang *et al.* (2001), where a manual intervention is required to determine the occurrence of a jet impact.

Once the nodes I and J are identified and the impact criterion has been satisfied, a so-called surgical-cut procedure can be performed following the descriptions of Zhang *et al.* (2001). Simply joining nodes I and J will not lead to a multiconnected fluid region, therefore nodes I and J will be deleted later in order to create a 'hole' where the jet impacts. This hole has to be made along the line connecting nodes I and J. Before deleting the two nodes, the remaining nodes will have to be reconnected. This is done in the following manner. The number of neighbouring nodes surrounding I and J is determined. If the two numbers are different, additional nodes will be added to make them identical. Then, these neighbouring nodes will be ordered, for jet and impact zone in the same systematic manner (for ease of joining). An arbitrary neighbour node of J on the jet tip will be chosen first, this node will be called m (see figure 2). A corresponding neighbour node of I on the impact zone will then be chosen in such a way that it is nearest to the jet tip node, let us call this node n. Nodes m and n will now be joined. This is done by moving both nodes m and n to a new position which is the average of the original vector positions of nodes m and n. All the other nodes on the jet tip will then be given a corresponding node on the impact zone with the help of the ordering and will be joined in a similar way to that described for nodes n and m. Finally, the nodes I and J and all the elements containing I or J are removed and some renumbering is performed. A typical completed surgical cut, performed on the bubble of figure 1, can be seen in figure 3.

Next, a vortex ring is placed inside the bubble, to take into account that the fluid domain is now no longer singly-connected. The vortex ring is also indicated in figure 3. The potential is now split into two parts, one associated with the potential of the vortex ring (generated by the jet impact), ψ, and a smooth remainder: φ,

$$\phi(\boldsymbol{x}, t) = \psi(\boldsymbol{x}) + \varphi(\boldsymbol{x}, t). \tag{15}$$

A discontinuity in the potential can be observed across this vortex ring. To be physically meaningful, this discontinuity must be equal to the jump in potential of the nodes of the jet and impact zone, I and J:

$$\Gamma = \phi_J - \phi_I. \tag{16}$$

The parameter Γ also determines the circulation of the flow. The vortex ring is placed entirely inside the bubble in such a way that the hole of the bubble is going through the ring. It is not necessary for the vortex ring to be in the plane of the impact surface. In our case, the ring is moved backwards (i.e. in the opposite direction of the jet velocity) in such a way, that it is situated well inside the bubble. Care must be taken in moving the ring in this way. If a node crosses over the ring, the smooth part of the potential must be changed by a value Γ. With the help of the Biot-Savart law, the velocity due to the vortex ring can be obtained on any node as:

$$\boldsymbol{u}_R(\boldsymbol{x}, t) = \frac{\Gamma}{4\pi} \oint \frac{\boldsymbol{r}(\boldsymbol{x}, \boldsymbol{x}') \times \mathrm{d}\boldsymbol{l}(\boldsymbol{x}')}{r^3}. \tag{17}$$

The integral is taken along the vortex ring; $\boldsymbol{r}(\boldsymbol{x}, \boldsymbol{x}')$ is a vector from a source point $\boldsymbol{x}'$ on the ring to a field point $\boldsymbol{x}$ under consideration and $r = \|\boldsymbol{r}\|$. The ring potential at any point $\boldsymbol{x}$ in the flow field or the bubble surface can be obtained by

$$\psi(\boldsymbol{x}) = \frac{\Gamma \Theta(\boldsymbol{x})}{4\pi}, \tag{18}$$

with

$$\Theta(\boldsymbol{x}) = \int_{S_c} \frac{\partial}{\partial n}\left(\frac{1}{r}\right) \mathrm{d}S \tag{19}$$

as the solid angle subtended at the point $\boldsymbol{x}$ by the surface of discontinuity S_c which extends over the vortex ring. The function $\Theta(\boldsymbol{x})$ entails a jump of 4π across S_c. Since the bubble is found to be mainly undergoing contraction and expansion, the normal velocity $\boldsymbol{u}_n = (\partial\varphi/\partial n)\boldsymbol{n} + (\boldsymbol{u}_R \cdot \boldsymbol{n})\,\boldsymbol{n}$ is used to perform the updating (instead of the EMT method). The vortex ring will remain unchanged, except for the occasional slight re-positioning to keep it well inside the bubble. The new boundary conditions on the bubble surface are (using again an Euler time-stepping scheme):

$$\boldsymbol{x}^{t+\delta t} = \boldsymbol{x}^t + \delta t\, \boldsymbol{u}_n, \tag{20}$$

and the remaining potential φ will be updated with:

$$\varphi^{t+\delta t} = \varphi^t + \delta t \left(1 - \tfrac{1}{2}\|\boldsymbol{u}_R + \nabla\varphi\|^2 - \delta^2 z - \varepsilon\left(\frac{V_0}{V}\right)^{\lambda} + \boldsymbol{u}_n \cdot (\boldsymbol{u}_R + \nabla\varphi)\right). \tag{21}$$

The system of equations resulting from (1) is still solved, but it is now applicable for the remainder potential φ and its normal derivative $\partial\varphi/\partial n$. The vortex ring also induces a potential and velocity on the structure. This velocity is not physical. This should not be reflected in the total potential ϕ and therefore a compensation in the smooth remainder potential, φ, should be made. The easiest way to do this is to apply a normal velocity $\partial\varphi/\partial n$ exactly opposite to the velocity caused by the vortex ring. This velocity will be implemented as a boundary condition on the structure in (1), in order for the correct physics to take place. It should be noted that, strictly speaking, the velocity of a resilient structure has to be incorporated in this boundary condition as well. However, the velocities on the structure are much lower than the velocities of the bubble and are therefore neglected, i.e. a zero normal velocity is

still assumed on the structure (as if the structure were rigid). This simplification is no longer permitted if the bubble oscillates with a frequency near the resonance frequency of the structure.

3.5. *Finite-element method (FEM) solver for the structural part and coupling with fluid part*

The structural part of the problem is simulated using the nonlinear FEM solver PAM-CRASH^{TM}. This commercial solver has been extensively used to simulate car crashes. Two options are available to couple the two codes; solving all the unknowns simultaneously (full coupling) or 'loose' coupling where the output of one code is used either as a boundary condition or a loading condition for the other. Since a 'loose' coupling has the advantage that only minor changes have to be made to both the structural and fluid (BEM) solver, this option has been chosen. In order to do so, forces on the nodes are calculated with the fluid code and given as input to the structural solver. The structural solver then calculates the displacements, which are returned as input for the fluid BEM solver. For the simulations to be described in § 4.4, the structural domain is first divided into a rectangular mesh consisting of one layer of sixty 8-noded brick elements and 146 nodes. The structure is assumed to behave as an elastic–plastic material (for more details, see the PAM-CRASH^{TM} Reference Manual 1997). An explicit time-integration scheme is used by the PAM-CRASH^{TM} solver to integrate the nonlinear equations of motion. On the boundary of the structure, proper load boundary conditions are given using the fluid solver. In order to do so, a second mesh consisting of sixty 4-noded shell elements (type: null material) is placed at the bottom of the mesh with the brick elements. These shell elements take on the forces supplied by the fluid solver. The displacements at the structure are then fed back to the fluid solver. The fluid solver uses a triangular mesh, created by dividing each of the 4-noded shells of the structural solver into two separate triangular shells. The two meshes, fluid mesh and structural shell mesh, need not be the same, therefore an interpolation function transfers back and forth the required parameters/information on the two meshes. In our calculations, however, the nodes are chosen to be identical for both meshes for ease of implementation. The load vector on the fluid mesh lying on the structure is obtained by first calculating the pressure on the structure with (3). This nodal pressure is then multiplied by the appropriate area of the surrounding elements of the respective node to arrive at the load vector.

An interface routine alternately calls the BEM and FEM solvers. The time steps of the two codes can be, and are usually, different. Therefore, a leapfrog time-advancing scheme is selected in the present work to cope with the different time steps of the fluid and solid codes. After each run of the BEM solver, it returns the time t_f pertaining to the fluid code. Then the FEM solver is called upon and returns the time t_s when it is ready for the next computation step. If $t_s < t_f$, the FEM solver will be called again until $t_s > t_f$. There is no need to include an added mass term in the mass-matrix of the structural solver, since the calculated pressure has automatically taken into consideration all the fluid-induced forces.

4. Computational results and discussions

4.1. *Preliminaries*

Though the numerical code can be simply called upon to simulate large-scale explosions such as a TNT charge of 500 kg, experiments are not so easily available to verify the calculations for these extreme cases. Even smaller-scale experiments are hard

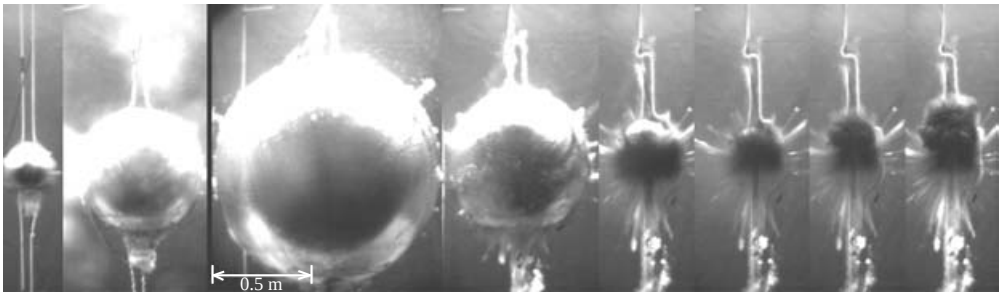

FIGURE 4. Explosion under free-field conditions: experimental results of a 55 g explosive charge; from left to right the bubble shape at: $t = 1$, 7, 50, 85, 93, 94, 95 and $t = 96$ ms. The second minimum volume occurs at $t = 94$ ms.

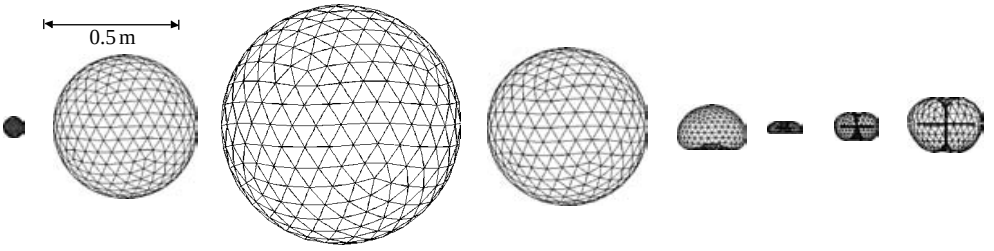

FIGURE 5. Explosion in a free-field configuration: numerical results of a 55 g explosive charge; from left to right at $t = 0$, 7.5, 50.2, 80.1, 89.1, 90.05, 90.61 and $t = 91.58$ ms. The second minimum volume occurs at $t = 90.05$ ms.

to come by. Therefore, a series of (controlled) small-scale tests have been performed with charges varying from 10 to 55 g (Hexocire explosive charges). First, several free-field tests are carried out in the absence of any nearby structures. Then, a charge will be placed near a vertical rigid wall. A charge under a horizontal resilient plate will be considered next. Finally, a test case will be shown, where the charge is placed at a slightly larger distance from a vertical rigid wall than in the previous arrangement.

4.2. *Explosions under free-field conditions*

The first series of experiments described are the free-field explosions. This means that there are no immediate boundaries (structures or free surfaces) near to the explosion bubble. Three charges of 10 g, 35 g and 55 g are used, placed at a depth of 3.5 m. The oscillating times and maximum bubble radii are different for the three bubbles, but their global behaviour is the same for the experiments as well as for the numerics. The experimental oscillation times for the three charges are 53, 82 and 94 ms for 10, 35 and 55 g, respectively. At roughly half of the oscillation time, the bubble reaches its maximum size. Experimental and numerical results for the three cases resemble each other qualitatively, therefore only a typical set of the results is shown. In figures 4 and 5, the bubble shapes for experiment and numerical simulations are shown, respectively, for a charge of 55 g. Note that for the experiments, the image of the bubble is the result of reflected light from the light sources in the set-up. The explosion happens at $t = 0$ ms. The white vertical lines visible in figure 4 are the supporting wires required to keep the charge in place before the explosion, these wires have also been placed horizontally in the experiments, to see if there is any influence on the bubble behaviour. No notable influence has been found. The bubble grows to its maximum

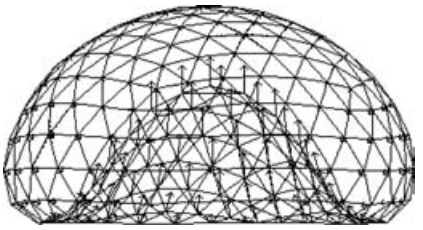

FIGURE 6. Bubble shape before jet impact for a 10 g explosive in a free-field configuration. The velocity vectors are also indicated.

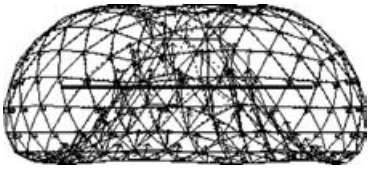

FIGURE 7. Bubble shape with jet impact at $t = 51.0$ ms, for a 10 g explosive in a free-field configuration.

radius measuring 56 cm at about $t = 50$ ms. As the nearest wall of the pond is at a distance of 3.0 m, it is reckoned that the influence from the walls of the pond and the free surface can be considered negligible. Furthermore, the walls are constructed with a step-like structure to minimize any coherent reflection. A jet can be observed to form in the last stages of the bubble collapse for the numerics. This jet is caused by the influence of gravity and develops at about $t = 85$ ms. No jet can be seen in this set of experimental results owing partly to some fuzziness of the pictures as well as the opaque bubble containing the dark-coloured combustion/explosion products which prevents us from clearly observing the jet development within the bubble. However, in other pictures some protrusion can be seen clearly on the top surface of the bubble near the bubble's minimum volume. Closer examination of figures similar to figure 4 at the later stages of the bubble evolution reveals the dark-coloured combustion products moving inwards with the jet from below and then being projected out of the topside of the bubble. This serves as 'indirect' evidence of the existence of the jet. In addition, the multi-directional 'spikes' extending from the dark coloured image of the spheroid bubble of the said later times may suggest the presence of solid particles arising from the explosion (probably un-burnt parts) which have made their way through the gaseous medium and into the water medium. Certainly, the particles, have vastly different inertia from the gaseous bubble and hence it is perhaps not unexpected that their resultant different momentum has given rise to this observed behaviour not captured numerically. Similar spikes have been observed in explosion bubbles by Tomita *et al.* (1994). They do not seem to appear in bubbles generated by different means (see for example Brujan *et al.* 2001*a*, *b* for laser generated bubbles). The minimum volume is reached at about $t = 90$ ms numerically and $t = 94$ ms experimentally. Figures 6 to 9 show the simulation of a 10 g charge just before and after jet impact; the event takes place at $t = 51.0$ ms numerically. The velocity vectors and the vortex ring are also shown. In figure 8, the bubble is depicted from a different angle (top view). In figure 9, the bubble is shown after it has reached its minimum volume, the bubble starts to re-expand. In figure 10, the volume of the bubble as a function of time is shown for both experimental and numerical results

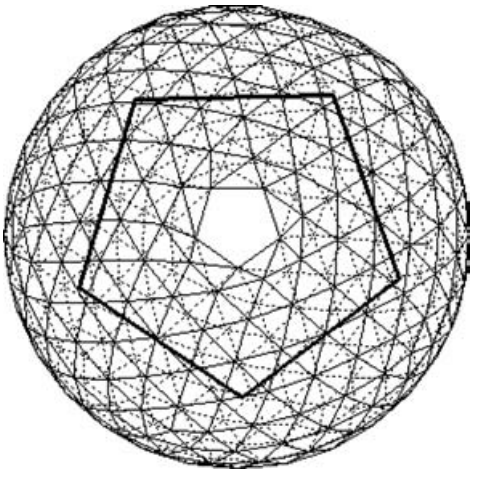

FIGURE 8. Top view of the toroidal bubble, with vortex ring and hole in the middle owing to jet impact at $t = 51.0$ ms, for a 10 g explosive in a free-field configuration.

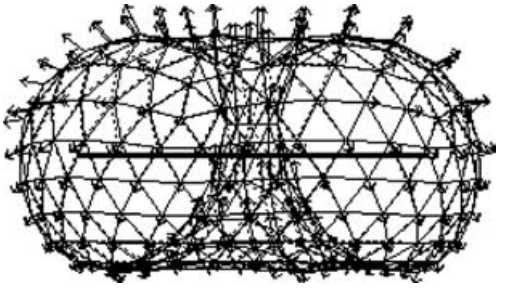

FIGURE 9. After the minimum volume, the bubble starts growing again, for a 10 g explosive in a free-field configuration.

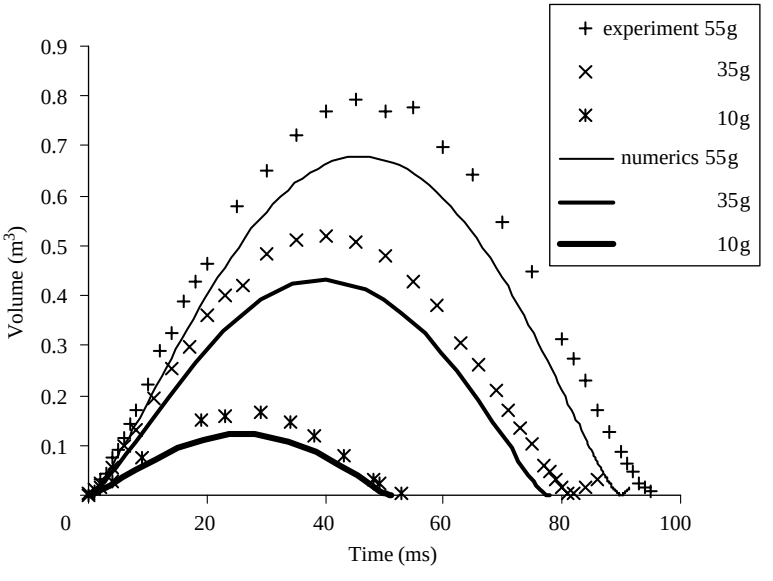

FIGURE 10. The evolution of the bubble volume, experimentally and numerically, for explosive charges of 10, 35 and 55 g under free-field conditions.

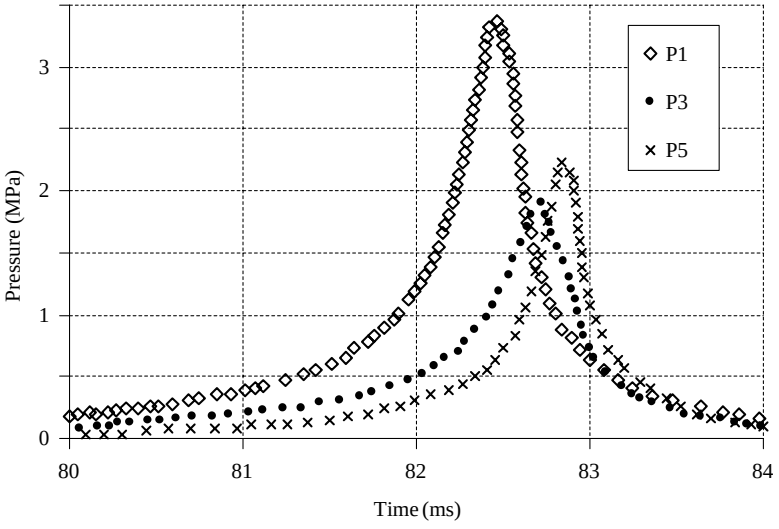

FIGURE 11. Experimental pressure profile around the second pressure peak (from 80 to 84 ms) for the explosive charge of 35 g at sensor positions P1, P3 and P5.

for the three charges. The experimental volume has been obtained by digitizing the image of the bubble and using the contrast of the light intensity level to determine the outline of the bubble for the diametrical plane (only the left-hand and right-hand boundaries of the bubble were considered, since the bottom boundary cannot be clearly distinguished). From there, an equivalent bubble diameter is obtained to produce the volume for comparison to the numerics. Of course, towards the final stages of the collapse, this will introduce increasing uncertainty in the experimental bubble volume, since the bubble is probably toroidal. Nevertheless, the broad comparison shows that the experimental volume is larger than the simulation and that the oscillation period (defined as the period between initiation and next minimum volume) is also slightly larger for the experiment with 55 g (91 *vs.* 94 ms). The observed trend can also be seen for the other charges of 10 g and 35 g (see figure 10). As could be expected, a larger charge will produce a larger maximum volume of the bubble; this volume is proportional to the charge weight (owing to energy considerations). The oscillation time is proportional to the maximum radius of the bubble (or to the cubic root of the charge weight) in both experiments and numerics. A possible explanation for the larger experimental maximum volumes and oscillation times could be that the calculations are based on TNT equivalent charges; the TNT equivalent of Hexocire in weight has been assumed to be 1.0. However, the equivalence is probably slightly larger, which will result in a larger bubble size and a larger oscillation period. This trend is reflected correctly with respect to the experimental data.

Pressure profiles were also measured as a function of time. For this purpose, some pressure sensors were placed in the flow at some distance from the charge. A sensor labelled P1 is placed beside the charge, at the same initial depth as the charge and at a horizontal distance of 0.7 m away from it. Two other pressure sensors were placed on top and below this sensor; P3 is at a horizontal distance of 0.7 m and a vertical distance of 0.71 m below the charge while P5 is at a horizontal distance of 0.7 m and a vertical distance of 1.095 m above the charge. A typical example of a pressure profile is shown in figure 11, where the experimentally measured pressure for times between 80 ms and 86 ms is shown for the three sensors for a charge of 35 g.

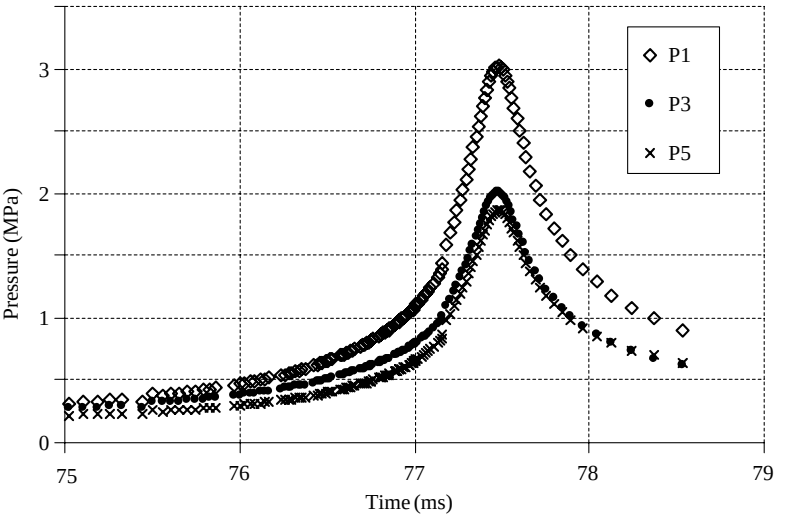

FIGURE 12. Numerical pressure profile at sensor positions P1, P3 and P5 for the explosive charge of 35 g; the numerical jet impact occurs at $t = 77.2$ ms.

This time span contains the jet impact and subsequent minimum bubble volume. The maximum pressure of P1 is the highest at about 3.3 MPa. This is as expected, since its location is nearest to the charge. This maximum occurs at about 82.5 ms. Sensor P3 gives a maximum pressure of 1.9 MPa and sensor P5 of 2.2 MPa. There is a time delay of about 0.5 ms between the maximum of sensor P1 and the other sensors. This is probably because the velocity of sound is finite and thus the high pressure will not be felt at the same instant at different places in the fluid. This is in contrast to the numerical method, which is supposed to be incompressible and therefore the pressure will be 'felt' immediately anywhere in the fluid domain. In figure 12, the numerical results are shown for pressure sensors placed at the same location as in the experiments. The maximum pressure of sensor P1 is 3.1 MPa, which is slightly lower than the observed experimental value. It occurs at 77.5 ms, which is earlier than recorded by the experiment. This can be expected since the numerical bubble oscillates slightly faster and will thus reach its maximum pressure earlier. The sensors P3 and P5 reach a maximum of 2.0 and 1.8 MPa, respectively, at about the same instant, the reason for this is explained above. Similar pressure profiles have been observed for the other charge weights (not shown here). The charge of 55 g gives the largest bubble size and tends to present the clearest experimental pictures. Therefore, for all other experiments described below, only the charge of 55 g will be considered.

4.3. *Explosion near a rigid vertical plate*

Next, a more complicated case is studied. A charge of 55 g is placed near a vertical rigid plate at a depth of 3.5 m. The plate has a dimension of 1.5 m $\times$ 1.5 m and is made of hardened steel. The thickness of the plate (5 cm) ensures that the plate remains essentially rigid. The standoff distance is 0.4 m, or 0.74 times the maximum bubble radius; this is found to be sufficiently close to attract the bubble towards the plate. In figures 13 to 16, the experimental and numerical bubble shapes can be seen. The solid plate is situated to the left-hand side of the bubble. The bubble starts expanding, but before it reaches its maximum size, it is already pushing against the wall. The bubble expands onto the wall considerably in this phase. When it collapses, it first takes on an urn-like shape and then develops a somewhat horizontal jet directed

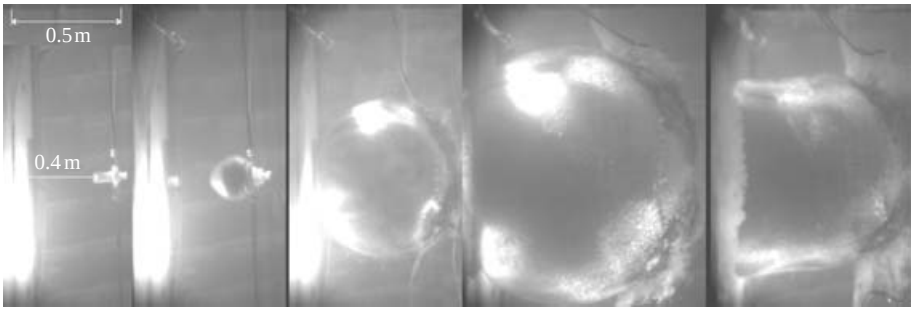

FIGURE 13. Explosion near a vertical rigid plate of a 55 g explosive charge. Experimental bubble shapes at $t < 0$, $t = 0$, 8, 50 and $t = 78$ ms.

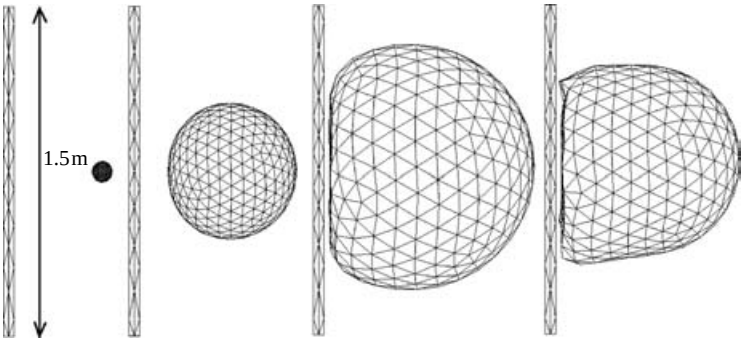

FIGURE 14. As for figure 13, numerical bubble shapes at $t = 0.0$, 6.7, 50.4 and $t = 74.8$ ms.

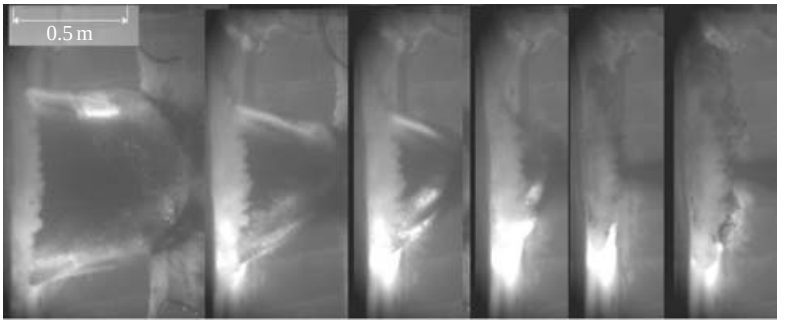

FIGURE 15. As for figure 13, experimental bubble shapes at $t = 82$, 91, 94, 97, 100 and $t = 104$ ms.

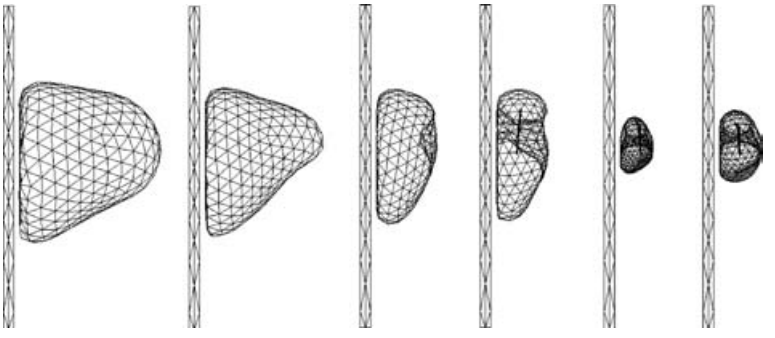

FIGURE 16. As for figure 13, numerical bubble shapes at $t = 85.8$, 89.4, 92.2, 93.2, 97.5 and 99.5 ms.

towards the plate (in the free-field cases the jet was directed upwards). It may be noted that the jet assumes a direction tilted slightly upwards during the initial phase of the toroidal shape which can be attributed to the combined effect of buoyancy (creating an upwards jet) and attraction to the wall (creating a jet directed towards the wall). The jet direction then seems to shift more and more perpendicular to the wall, probably indicating that the attraction effect of the wall becomes greater and greater as the centroid of the bubble moves increasingly closer to the plate. The numerical bubble shapes correspond very well with the observed experimental data. Again, in the last stages of the collapse, the experimental data become very fuzzy and no jet formation can be directly observed. In the experiment, the oscillation time is 100 ms, while in the simulation it is 97.5 ms.

4.4. *Explosion below a resilient horizontal plate*

The subject of oscillating bubbles near a resilient structure has not been studied extensively in literature. Brujan *et al.* (2001*a*, *b*) present some experimental data concerning millimetre sized bubbles near a gel-like material. Klaseboer & Khoo (2004) have subsequently carried out a numerical study on the same subject for an axisymmetric bubble configuration. An approach closely resembling the work of Duncan, Milligan & Zhang (1996) will be followed in this work. They simulated the interaction between a bubble and a compliant structure using a coupling between a boundary-element code for the fluid and a finite-element code for the structure. This, among others, was used to simulate the experimental data of Shima *et al.* (1989) of a bubble near a solid wall with an elastic coating. More experimental results on this subject were presented in Tomita & Kodama (2003).

In the next case, an explosive of 55 g is placed under a sufficiently thin circular resilient steel plate with a diameter of 0.6 m and thickness of only 2 mm. The circular plate is placed horizontally with fluid loading on the bottom side (the other side is air-backed). The steel plate has the following mechanical properties: the density is 7800 kg m^{-3}, the shear modulus is 80.7 GPa, the tangent modulus is 0.4038 GPa, the bulk modulus is 175 Gpa, the yield stress is 240 MPa, Young's modulus is 210 GPa and the Poisson ratio is 0.3. This thickness of 2 mm is thin enough to allow relatively large deformations of the plate to occur. The plate has been fixed at its boundaries for all six degrees of freedom. The standoff distance has been chosen to be 1.2 m below the plate (or 2.2 times the maximum bubble radius of 0.54 m). The distance between the explosive charge and the floor of the pond is 3.5 m (the charge depth is also 3.5 m). In the experiment, several displacement sensors are used to record the deformation of the steel plate. Since the standoff distance is larger than the bubble radius, the bubble behaves, to some extent, like a free-field bubble. The jet is directed upwards and towards the plate. The simulation is stopped once the results of the PAM-CRASH^{TM} code indicate very little or no change anymore, which is taken to be the final deformation of the structure.

Both the simulation and experiment can be seen in figure 17 where the initial maximum bubble size and subsequent minimum bubble size are shown. The extent of the plate is rather small compared to the maximum bubble radius. In figure 18, the deformation of the centre of the plate is shown as a function of time. Both curves, experimentally and numerically, start with an initial deformation of zero. Note that the deformation shows minimal changes at $t \approx 100$ ms and beyond. Experimentally, the movement of the supporting structure holding the plate has been properly accounted for to arrive at the displacement of the plate centre relative to the (fixed) edge. The centre of the plate moves away from the bubble very rapidly (positive displacement)

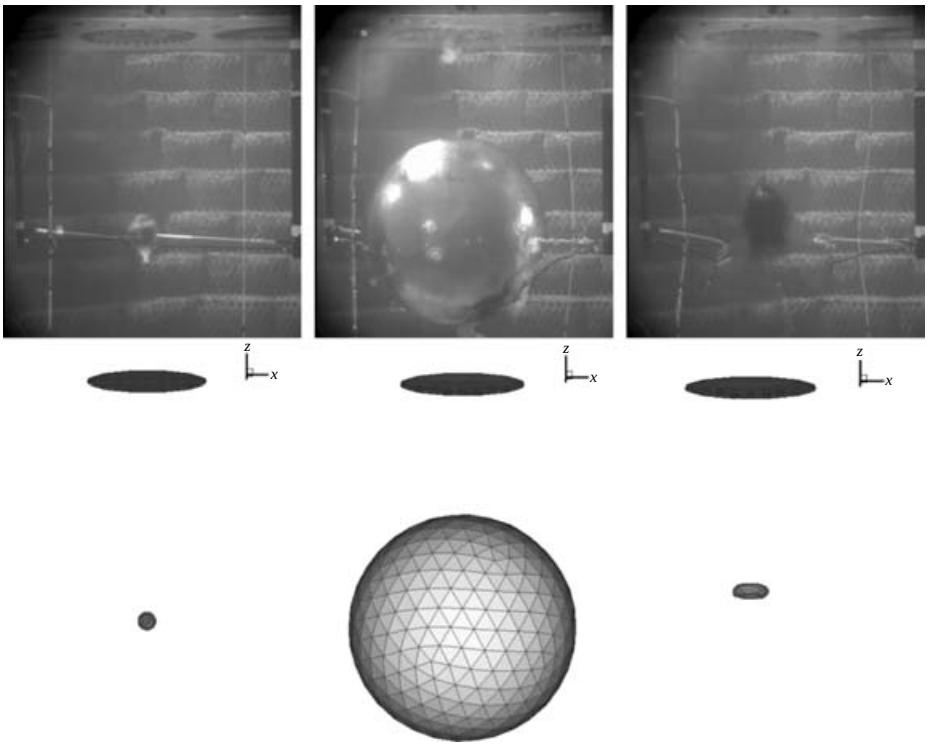

FIGURE 17. Explosion below a resilient plate for a 55 g explosive charge: (*a*) experimental and (*b*) numerical results; from left to right at $t = 0$ ms (experimental and numerical), 45 ms (experimental and numerical), 91 ms (experimental) and 90 ms (numerical).

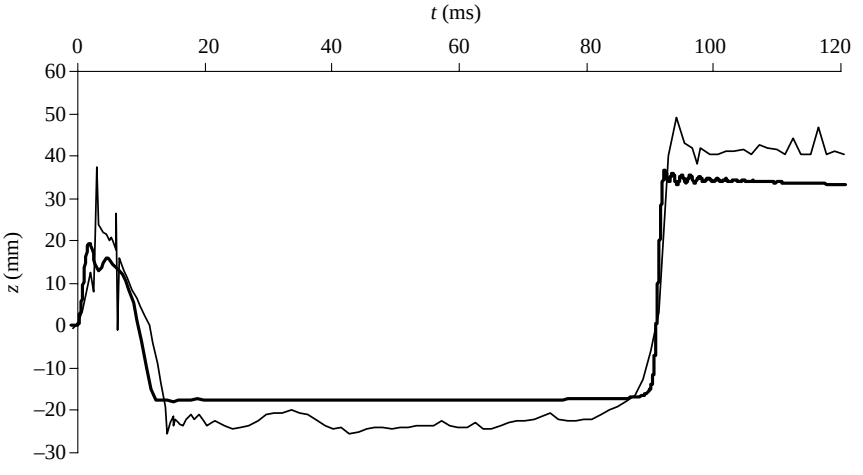

FIGURE 18. Displacement z of the centre of the plate relative to its edge as a function of time; numerical (thick line) and experimental (thin line). A positive displacement means that the plate is moving away from the bubble.

immediately after the explosion. In only a few milliseconds, it moves to a displacement of 30 mm. It then quickly reverses direction and moves towards the bubble within about 10 ms. This can partly be explained by the fact that the bubble pressure very

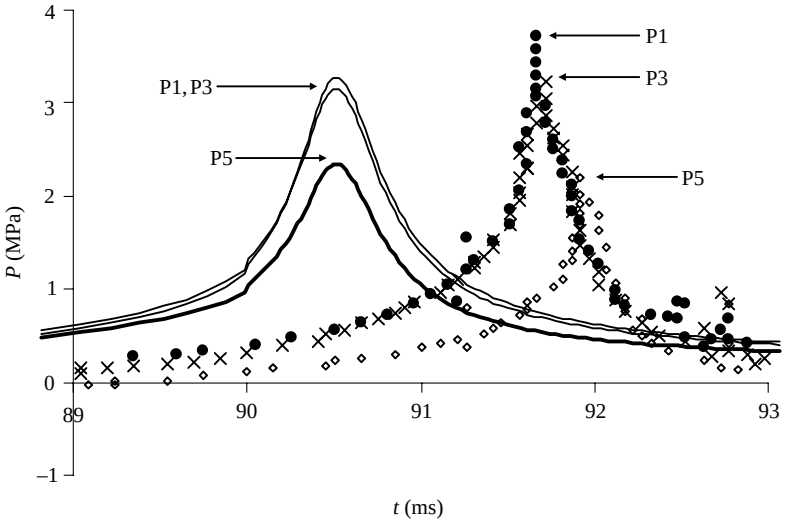

FIGURE 19. Numerical (solid lines) and experimental (symbols) pressure profile for the sensors P1 (highest peak magnitude), P3 (moderate peak magnitude) and P5 (lowest peak magnitude).

soon becomes lower than the surrounding pressure, thus creating a suction effect exerted on the plate. The plate then stays a relatively long time, for about 80 ms, in this position amidst some limited transient movement observed. When the bubble finally collapses, the pressure caused by the ensuing jet and the compressed gas inside the bubble eventually leads to the permanent (and plastic) deformation of the plate; this deformation of 40 mm is larger than that observed just after the explosion (about 20 mm, see figure 18). The numerical results are similar in behaviour. The experimental deformation is larger than the numerics: the permanent deformation from the numerics is 34 mm compared to the experiment at 40 mm. One possible reason behind the noted difference is: the neglect of the influence of the shock wave in the numerical model which is estimated to contribute an error of about 10 % (see below on the discussion on the pressure results). The supporting structure is not included in the numerical model; it could give rise to a larger pressure on the plate. All these will lead to a lower numerical net force acting on the plate structure. It is therefore not too surprising to observe a discrepancy of about 15 % larger in the final deformation of the plate centre in the experiment. From Amabili & Kwak (1996), the fundamental eigenfrequency of the fluid-loaded circular plate is 97 Hz. This frequency is much higher than the typical frequency of the bubble (around 10 Hz).

Further examination of some pressure measurements from the time of 89 ms to 93 ms thereby encompassing the second pressure peak at around 91 ms for the experiment is shown in figure 19. The pressure sensor P1, is placed at a horizontal distance of 70 cm from the initial position of the explosive charge. Sensor P3 is placed 30 cm above sensor P1 and sensor P5 is placed 50 cm below sensor P1. The numerical pressure corresponds reasonably well with that observed in the experiment: the maximum peak for sensor P1 is 3.7 MPa (experiment) and 3.2 MPa (numerical); for sensor P3 3.1 MPa (experiment) versus 3.2 (numerical); for sensor P5, 2.2 MPa is found for experiment and 2.3 MPa for the simulation. The two numerical curves P1 and P3 are almost indistinguishable. Experimentally, the pressure immediately after the explosion registers a very large value. For example, a pressure sensor at the centre of the plate measures a peak pressure close to 30 MPa, which is attributed to the

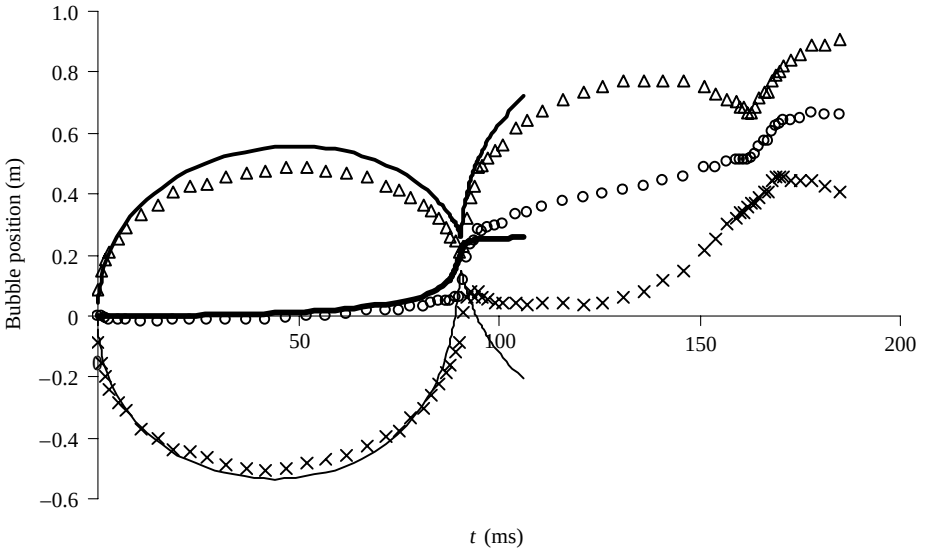

FIGURE 20. The position of the upper bubble surface, the lower bubble surface and centre of mass as a function of time for the case of figure 17; experimental: triangles (upper bubble surface), circles (centre of mass) and crosses (lower bubble surface); numerical: thin continuous line (lower), medium continuous line (upper) and thick continuous line (centre of mass).

shock wave. It very rapidly decreases to 5 MPa in only about 0.1 ms and further decreases to 1 MPa within 0.5 ms. An estimation of the integral of the pressure profile with time from 30 to about 10 MPa (the latter is associated with the bubble pressure assuming dominance as implied from the numerics) gives us a value of 5. A similar integral carried out for the numerical results from a maximum value of about 10 down to 0.1 MPa gives a value of about 30. Since there is another or second bubble pulse (associated with the jet impact) with a fairly similar pressure profile, this would combine to a total integral value of 60 owing to the bubble dynamics. The influence of the shock wave in the final deformation of the plate is thus estimated to be about 10 %, based broadly on the ratio of the pressure integrals associated with the shock to the bubble dynamics. It is not possible to distinguish the pressure induced by the shock from that generated by the bubble in the experimental results. Therefore, no comparison is shown here between the experimental and numerical pressures at those times just after the explosion.

An interesting feature is also the position of the bubble as a function of time. In figure 20, the position of the upper bubble surface, the lower bubble surface and the centre of mass (average of the above) are plotted for both experiment and numerics. The upper and lower bubble surfaces show a typical oscillation due to the volume fluctuation of the bubble. The centre of mass is rising sharply when the bubble reaches its second minimum volume around 90 ms. At $t = 96$ ms, the experimental centre of mass has reached a value of 0.28 m; in the numerical results, it reaches a slightly lower value of 0.25 m. In the experiments, the bubble then continues to oscillate, but with a lower amplitude due to energy losses. It reaches a third minimum volume at $t = 165$ ms. Since in the numerical results, no energy losses are taken into account, the numerical bubble rebounds with a relatively larger intensity (in future works, this energy loss should be taken into consideration). However, since the main 'loading' due to the bubble occurs around the second minimum volume (as shown in the pressure plots

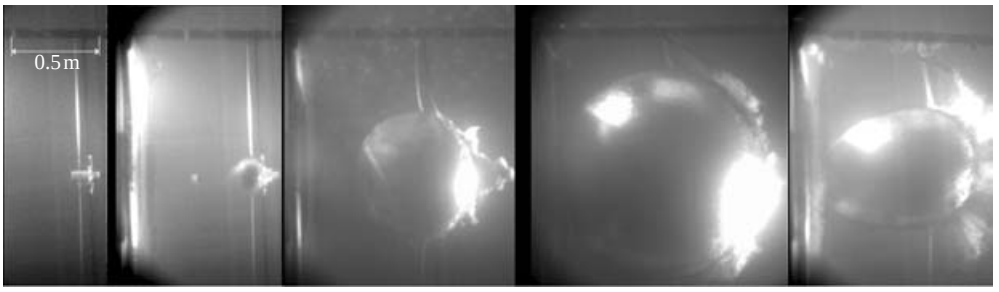

FIGURE 21. Explosion near a vertical rigid plate of a 55 g explosive charge at a stand-off distance of 0.6 m. Experimental results at $t = 0$, 8, 48 and 86 ms.

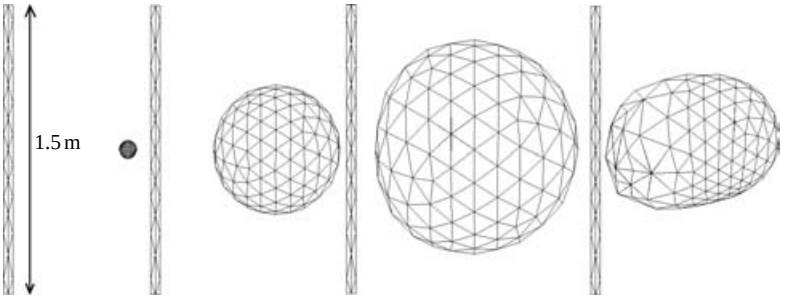

FIGURE 22. As for figure 21, numerical results at $t = 0$, 8.2, 44.6 and 83.4 ms.

of figure 19), the uncertainty/error associated with the numerical displacement of the plate should not be significant. Another illustration of the energy losses encountered in the experiments can be found in figure 19, where the experimental pressure profiles are non-symmetric with respect to the peak value. In other words, the pressure drops much faster after the peak than it rises before the peak. This is in contrast to the numerical results, where the pressure pulse is symmetric around the peak value. It can be seen that a similar bubble produced under free-field conditions, as in figure 4, gives rise to an almost identical plot as shown in figure 20 regarding the positions of the upper and lower bubble surface and centre of mass (not shown here). This also indicates that the bubble behaves as a free-field bubble, which is attributed to the sufficiently large distance between the plate and the bubble. The bubble moves mainly under the influence of gravity in this case.

4.5. *Explosion at a larger standoff distance*

The last case under consideration is for a charge of 55 g placed beside a vertical rigid plate at a relatively large standoff distance of 0.6 m (or 1.1 times the maximum bubble radius) and a depth of 3.5 m. The same rigid plate as in § 4.3 is used. Since the standoff distance is larger than that found in § 4.3, the influence of gravity can be seen more clearly. In figures 21 and 23, the experimental results are presented with the rigid wall on the left-hand side of the bubble. The numerical results at comparable times are shown in figures 22 and 24. The bubble grows until it reaches its maximum size at about $t = 48$ ms experimentally. A flattening of the bubble surface can be observed, where it is nearest to the plate. It is also found that the experiment takes a slightly longer time to reach a similar level of bubble evolution compared to the

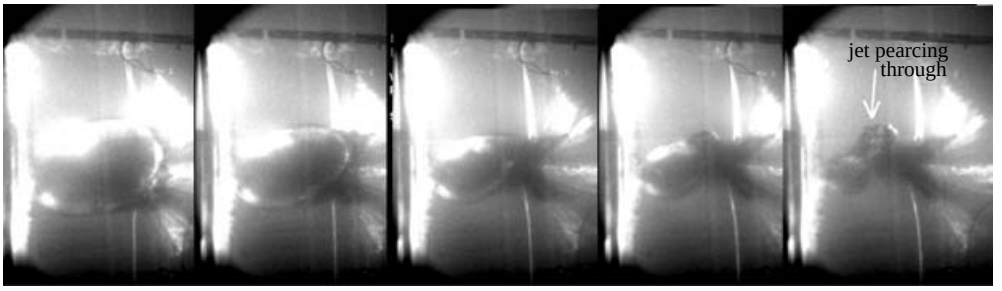

FIGURE 23. As for figure 21, experimental results at $t = 90$, 92, 94, 95 and 96 ms.

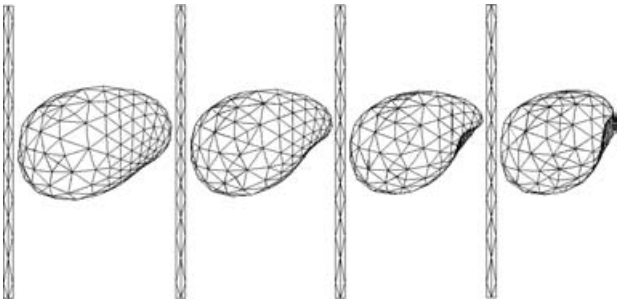

FIGURE 24. As for figure 21, numerical results at $t = 88.5$, 90.10, 90.93 and 91.7 ms.

numerics. In the collapse phase, the bubble initially assumes an egg shape. Then, a jet is seen developing at the extreme end of the bubble, furthest away from the wall in the simulation. This jet is likely to make an impact on the top right-hand surface of the bubble, as depicted in the last image of figure 23. In the experiment, the explosive products can be seen to 'pierce' through the top section of the bubble obliquely and project into the water medium above the bubble. Had the standoff distance been chosen to be larger, say twice the maximum bubble radius, then gravity would have dominated the problem and similar situations as discussed in § 4.2 would appear with a gravity jet pointing upwards fairly symmetrically (see also Blake & Gibson 1987). Overall, the comparison between experiment and simulation has been fair, at least for the shapes of the bubble development.

5. Conclusions

The present paper shows the results of a comparison between experiment and a coupled BEM-FEM simulation of three-dimensional interactions between an underwater explosion bubble and a nearby submerged structure in various geometrical arrangements. This is one of the few occasions where controlled experiments on an underwater explosion with fairly large charges ranging from 10 g to 55 g of Hexocire were used and data made available in the literature. The fluid domain is calculated with the BEM method, while the structure domain is discretized by FEM. The BEM and FEM share the same displacement and force on the common boundary between structure and fluid (the wetted surface). The present approach can handle the nonlinear property of the structure, such as large plastic deformation. The comparisons have been fair, which also serves to validate the present method.

The authors would like to thank both DSO National Laboratories (Singapore) and Service des Programmes Navals (France) for their support, which made this work possible.

REFERENCES

Amabili, M. & Kwak, M. K. 1996 Free vibrations of circular plates coupled with liquids: revising the Lamb problem. *J. Fluid Struct.* **10**, 743–761.

Blake, J. R. & Gibson, D. C. 1981 Growth and collapse of a vapour cavity near a free surface. *J. Fluid Mech.* **111**, 123–140.

Blake, J. R. & Gibson, D. C. 1987 Cavitation bubbles near boundaries. *Annu. Rev. Fluid Mech.* **19**, 99–123.

Brett, J. M., Yiannakopoalos, G. & Schaaf, P. J. 2000 Time-resolved measurement of the deformation of submerged cylinders subjected to loading from a nearby explosion. *Intl J. Impact Engng* **24**, 875–890.

Brujan, E.-A., Nahen, K., Schmidt, P. & Vogel, A. 2001*a* Dynamics of laser-induced cavitation bubbles near an elastic boundary. *J. Fluid Mech.* **433**, 251–181.

Brujan, E.-A., Nahen, K., Schmidt, P. & Vogel, A. 2001*b* Dynamics of laser-induced cavitation bubbles near elastic boundaries: influence of the elastic modulus. *J. Fluid Mech.* **433**, 283–314.

Chahine, G. L., Frederick, G. S., Lambrecht, C. J., Harris, G. S. & Mair, H. U. 1995 *SAVIAC Proceedings 66th Shock and Vibrations Symposium, Biloxi, MS*, vol. 2, pp. 265–276.

Cole, R. H. 1948 *Underwater Explosions*. Princeton University Press.

Duncan, J. H., Milligan, C. D. & Zhang, S. 1996 On the interaction between a bubble and a submerged compliant structure. *J. Sound Vib.* **197**, 17–44.

Harris, P. J. 1992 A numerical model for determining the motion of bubble close to a fixed rigid structure in a fluid. *Intl J. Num. Methods Engng* **33**, 1813–1822.

Klaseboer, E. & Khoo, B. C. 2004 An oscillating bubble near an elastic material. *J. Appl. Phys.* **96**, 5808–5818.

Lundgren, T. S. & Mansour, M. N. 1991 Vortex ring bubbles. *J. Fluid Mech.* **224**, 177–196.

Oguz, H. N. & Prosperetti, A. 1990 Bubble entrainment by the impact of drops on liquid surface. *J. Fluid Mech.* **219**, 143–179.

Pamcrash, 1997 *Pamcrash Solver Reference Manual.* Pam System International SA.

Popinet, S. & Zaleski, S. 2002 Bubble collapse near a solid boundary: a numerical study of the influence of viscosity *J. Fluid Mech.* **464**, 137–163.

Rungsiyaphornrat, S., Klaseboer, E., Khoo, B. C. & Yeo, K. S. 2003 The merging of two gaseous bubbles with an application to underwater explosions. *Comput. Fluids* **32**, 1049–1047.

Shima, A., Takayama, K. & Tomita, Y. 1984 Mechanism of the bubble collapse near a solid wall and the induced impact pressure generation. *Rep. Inst. High Speed Mech.* **48**, 77–97.

Shima, A., Tomita, Y., Gibson, D. C. & Blake, J. R. 1989 The growth and collapse of cavitation bubbles near composite surfaces. *J. Fluid Mech.* **203**, 199–214.

Tipton, R. E., Steinberg, D. J. & Tomita, Y. 1992 Bubble explosion and collapse near a rigid wall. *JSME Intl J. Series II* **35**, 67–75.

Tomita, Y. & Kodama, T. 2003 Interaction of laser-induced cavitation bubbles with composite surfaces. *J. Appl. Phys.* **94**, 2809–2816.

Tomita, Y., Obara, T., Takayama, K. & Kuwahara, M. 1994 Cavitation phenomena in extracorporeal microexplosion lithotripsy. *Shock Waves* **3**, 149–157.

Tomita, Y. & Shima, A. 1994 Interactive problems in bubble dynamics. *Current Topics Acoust. Res.* **1**, 231–246.

Tomita, Y., Shima, A. & Takahashi, K. 1983 The collapse of a gas bubble attached to a solid wall by a shock wave and the induced impact pressure. *J. Fluids Engng* **105**, 341–349.

Tomita, Y., Shima, A. & Takahashi, H. 1991 The behaviour of a laser-produced bubble near a rigid wall with various configurations. *ASME 1991, Cavitation '91, FED-* **116**, 19–25.

Tomita, Y., Shima, A., Tsubota, M. & Kano, I. 1994 An experimental investigation on bubble motion in liquid nitrogen. *The 2nd Intl Symp. on Cavitation, Tokyo, Japan*, pp. 311–316.

Tong, R. P. 1997 A new approach to modeling an unsteady free surface in boundary integral methods with application to bubble–structure interactions. *Math. Comput. Sim.* **44**, 415–426.

Wang, C., Khoo, B. C. & Yeo, K. C. 2003 Elastic mesh technique for 3D BIM simulation with an application to underwater explosion bubble dynamics. *Comput. Fluids* **32**, 1195–1212.

Wang, Q. X. 1998 The evolution of a gas bubble near an inclined wall. *Theoret. Comput. Fluid Dyn.* **12**, 29–51.

Wang, Q. X., Yeo, K. S., Khoo, B. C. & Lam, K. Y. 1996 Nonlinear interaction between gas bubble and free surface. *Comput. Fluids* **25**, 607.

Zhang, S. G., Duncan, J. H. & Chahine, G. L. 1993 The final stage of the collapse of a cavitation bubble near a rigid wall. *J. Fluid Mech.* **257**, 147–181.

Zhang, S. G. & Duncan, J. H. 1994 On the non-spherical collapse and rebound of a cavitation bubble. *Phys. Fluids* **6**, 2352–2362.

Zhang, Y. L., Yeo, K. S., Khoo, B. C. & Chong, W. K. 1998 Three-dimensional computation of bubbles near a free surface. *J. Comput. Phys.* **146**, 105–123.

Zhang, Y. L., Yeo, K. S., Khoo, B. C. & Wang, C. 2001 3D jet impact and toroidal bubbles. *J. Comput. Phys.* **166**, 336–360.